J. Fluid Mech. (2011), *vol.* 679, *pp.* 101–121.
doi:10.1017/jfm.2011.125

A lattice Boltzmann study on the drag force in bubble swarms

J. J. J. GILLISSEN[1]†, S. SUNDARESAN[2] AND H. E. A. VAN DEN AKKER[1]

[1]Department of Multi-Scale Physics, J. M. Burgers Centre for Fluid Mechanics, Delft University of Technology, Prins Bernhardlaan 6, 2628 BW Delft, The Netherlands

[2]Department of Chemical Engineering, Princeton University, Princeton, NJ 08544, USA

(Received 6 July 2010; revised 21 January 2011; accepted 9 March 2011; first published online 9 May 2011)

Lattice Boltzmann and immersed boundary methods are used to conduct direct numerical simulations of suspensions of massless, spherical gas bubbles driven by buoyancy in a three-dimensional periodic domain. The drag coefficient C_D is computed as a function of the gas volume fraction ϕ and the Reynolds number $Re = 2RU_{slip}/\nu$ for $0.03 \lessapprox \phi \lessapprox 0.5$ and $5 \lessapprox Re \lessapprox 2000$. Here R, U_{slip} and ν denote the bubble radius, the slip velocity between the liquid and the gas phases and the kinematic viscosity of the liquid phase, respectively. The results are rationalized by assuming a similarity between the $C_D(Re_{eff})$-relation of the suspension and the $C_D(Re)$-relation of an individual bubble, where the effective Reynolds number $Re_{eff} = 2RU_{slip}/\nu_{eff}$ is based on the effective viscosity ν_{eff} which depends on the properties of the suspension. For $Re \lesssim 100$, we find $\nu_{eff} \approx \nu/(1-0.6\phi^{1/3})$, which is in qualitative agreement with previous proposed correlations for C_D in bubble suspensions. For $Re \gtrsim 100$, on the other hand, we find $\nu_{eff} \approx RU_{slip}\phi$, which is explained by considering the turbulent kinetic energy levels in the liquid phase. Based on these findings, a correlation is constructed for $C_D(Re, \phi)$. A modification of the drag correlation is proposed to account for effects of bubble deformation, by the inclusion of a correction factor based on the theory of Moore (*J. Fluid Mech.*, vol. 23, 1995, p. 749).

Key words: bubble dynamics, gas/liquid flows, turbulence simulation

1. Introduction

We examine the drag force acting on a statistically homogeneous and statistically steady assembly of monodisperse gas bubbles rising in a liquid under the action of buoyancy.

In experiments, breakup and coalescence of bubbles result in a dynamic distribution of bubble sizes, and inhomogeneous distributions of bubbles arise due to wall effects. Furthermore at large gas volume fraction, the homogeneous bubbly flow transitions to heterogeneous bubbly flow, which is characterized by a strong coupling between large scale fluid circulation and bubble coalescence (Harteveld, Mudde & Van Den Akker 2003). In addition, small amounts of impurities in the carrying liquid can have large effects on the bubble dynamics. For instance, Maxworthy *et al.* (1996) used mixtures

† Email address for correspondence: j.j.j.gillissen@tudelft.nl

of triply distilled water and glycerin and measured a 30 % larger drag coefficient than Duineveld (1995) who performed experiments in 'hyper clean water'.

In simulations, the above mentioned complexities can be excluded which provides a way to gain insight into the essential dynamics. In this work, we use numerical simulations of highly idealized systems and use the results to construct a model for the drag coefficient in bubble swarms.

In the present analysis, we ignore effects of walls and polydispersivity. In this way, the problem can be reduced to relating the drag coefficient C_D,

$$C_D = \frac{\frac{4}{3} R\,(1-\phi)\,g}{U_{slip}^2}, \tag{1.1}$$

to three independent, dimensionless parameters. These parameters are chosen to be the gas volume fraction ϕ, the bubble Reynolds number,

$$Re = \frac{U_{slip} 2R}{\nu}, \tag{1.2}$$

and the bubble Weber number,

$$We = \frac{\rho U_{slip}^2 2R}{\sigma}. \tag{1.3}$$

Here g is the gravitational acceleration, ρ is the liquid mass density, U_{slip} is the velocity difference between the gas and the liquid, ν is the liquid kinematic viscosity, σ is the surface tension of the gas–liquid system and $R = (3V_B/4\pi)^{1/3}$ is the bubble equivalent radius, where V_B is the bubble volume. The relation for the drag coefficient (1.1) is derived in the Appendix.

For uniform flow around a spherical bubble with free-slip boundary conditions at the bubble surface, Mei & Klausner (1992) proposed the following $C_D(Re)$-correlation that asymptotically matches the theoretical cases of $Re \ll 1$ and $Re \gg 1$ as well as accurately approximates numerical simulation data in the intermediate regime:

$$C_D = \frac{16}{Re}\left\{1 + \left[\frac{8}{Re} + \frac{1}{2}\left(1 + 3.315 Re^{-(1/2)}\right)\right]^{-1}\right\}. \tag{1.4}$$

Departure from the spherical shape occurs when the hydrodynamic forces acting on the bubble surface exceed the surface tension forces, i.e. when $We \gtrsim 1$. For air bubbles rising in water, significant departure from the spherical shape to the ellipsoidal shape is expected when the bubble radius exceeds a value of $R \approx 0.5$ mm (Duineveld 1995), corresponding to an aspect ratio $\chi \approx 1.2$, a Weber number of $We \approx 1$ and a Reynolds number of $Re \approx 260$, respectively. At larger $We \approx 2.5$, when the bubble aspect ratio exceeds $\chi \approx 1.7$, a recirculation wake develops (Blanco & Magnaudet 1995). In the air–water system, this corresponds to $R \approx 0.7$ mm and $Re \approx 520$. By increasing We even further, the bubble shape transitions from ellipsoidal to spherical cap (Maxworthy *et al.* 1996). Assuming that the bubble shape is ellipsoidal and that there is no recirculating wake, Moore derived a relation between We and the bubble aspect ratio χ ((1.5) in Moore 1965) as well as the leading order correction G to the drag coefficient as a function of χ ((2.12) in Moore 1965). Combining these relations gives a relation between G and We, which for $We < 3.5$ can accurately be

approximated by

$$G = \left[1 - \left(\frac{We}{4}\right)^{1.16}\right]^{-0.92}. \tag{1.5}$$

Including this factor into (1.4) gives the following expression for C_D in terms of Re and We for an individual deformable gas bubble:

$$C_D = \left[1 - \left(\frac{We}{4}\right)^{1.16}\right]^{-0.92} \frac{16}{Re}\left\{1 + \left[\frac{8}{Re} + \frac{1}{2}\left(1 + 3.315Re^{-(1/2)}\right)\right]^{-1}\right\}. \tag{1.6}$$

Equation (1.6) is valid in the absence of a recirculating wake, which for the air–water system is up to $We \approx 2.5$. Within this range (1.6) is within 15 % of the experimental data of Duineveld (1995). While the C_D for an individual rising gas bubble can be captured reasonably well by a relation such as (1.6), there is to date no equivalent relation for bubble swarms.

The aim of the present paper is to propose a C_D-relation that captures and thereby provides insight into the dynamics of rising bubble swarms over a wide range of ϕ and Re. The complexity of bubble swarms at large Re stems from the combination of bubble deformation and random velocity fluctuations in the interstitial liquid, referred to as pseudo-turbulence.

We tackle this complexity in two steps. First we ignore bubble deformation and conduct direct numerical simulations (DNS) of spherical gas bubbles. From the simulation data, we derive a $C_D(Re, \phi)$-relation where the role of the pseudo-turbulence is incorporated via an effective viscosity. Second, we extend the model to account for bubble deformation by including the distortion factor G (1.5) into the expression for C_D. The final result constitutes a $C_D(Re, \phi, We)$-relation. This relation is tested against experimental data from the literature.

Previous DNS studies on bubble suspensions (see for instance: Esmaeeli & Tryggvason 2005; Van Sint Annaland *et al.* 2006) focused on shape deformations and higher order velocity statistics, but the relation between C_D, ϕ, Re and We has not yet been systematically explored. To our knowledge, the widest parameter range that has been explored using DNS is due to Yin & Koch (2008), who studied systems of spherical gas bubbles for $5 < Re < 20$ and $0 < \phi < 0.25$. Sangani & Didwania (1993) used potential flow simulations to analyse spherical bubble suspensions at $Re \approx 500$. These simulations predicted a strong tendency of bubbles to cluster in horizontal planes. The effect of fluid vorticity, which is excluded in their potential flow calculations, on such clustering remains unexplored.

2. Numerical method

2.1. *Governing equations*

In this work, we simulate the buoyancy-driven rise of spherical gas bubbles in a three-dimensional periodic volume V. Gravity acts on the system in the negative x-direction. The volume is decomposed into a volume containing the liquid phase V_L with a mass density ρ and a volume containing the gas phase V_G with a negligible mass density; $V = V_L + V_G$. The gas phase consists of N_B spherical bubbles of radius R. Elastic, hard-sphere collisions of the bubbles are assumed (Chen, Kontomaris & McLaughlin 1998). To illustrate the computational setup, we have provided in figure 1 contour plots of the fluid velocity in a vertical cross-section of the computational domain.

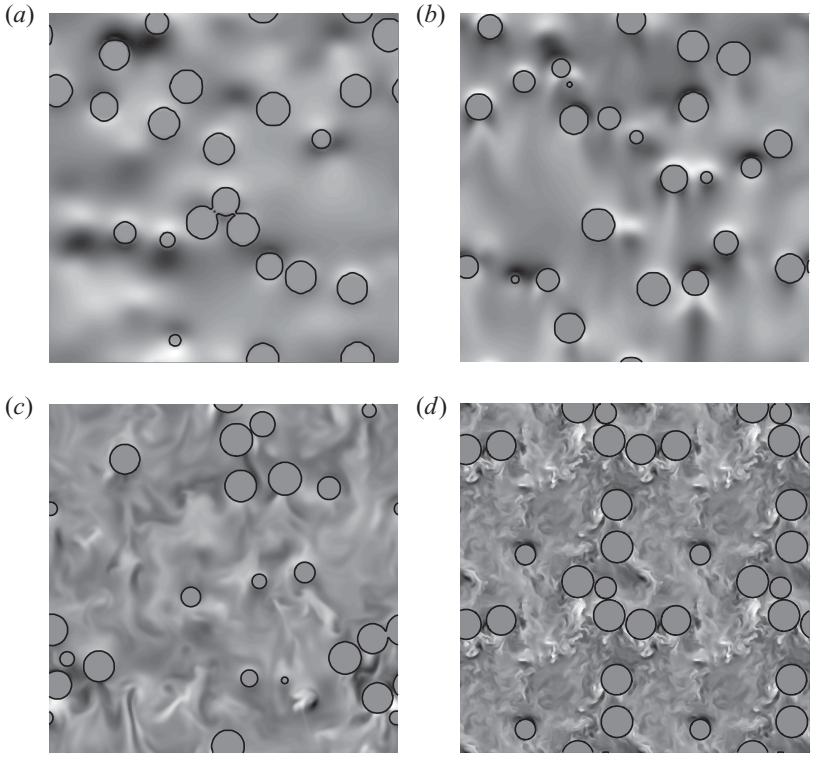

FIGURE 1. Fluid velocity component normal to the plane of view u_y for $\phi = 0.11$ and $Re \approx 5$ (a), $Re \approx 50$ (b), $Re \approx 500$ (c) and $Re \approx 2000$ (d). Black and white correspond to negative u_y and positive u_y, respectively. For clarity, we set $u_y = 0$ in the bubbles. For $Re \approx 5$, $Re \approx 50$ and $Re \approx 500$, the linear domain size is $L/R = 21\frac{1}{3}$, while for $Re \approx 2000$ the linear domain size is $L/R = 10\frac{2}{3}$. For clarity, we show this latter case on an equal domain size as the other cases by displaying four periodic images of the same field. Gravity is pointing down. The circles in the figure indicate the cross-sections of the bubbles with the plane.

The flow inside the liquid phase is described by the continuity equation,

$$\nabla \cdot \boldsymbol{u} = 0, \quad \forall \boldsymbol{x} \in V_L, \tag{2.1a}$$

and the incompressible Navier–Stokes equation,

$$\rho \left(\frac{\partial \boldsymbol{u}}{\partial t} + \boldsymbol{u} \cdot \nabla \boldsymbol{u} \right) = -\phi \rho g \boldsymbol{e_x} + \nabla \cdot (-p\boldsymbol{\delta} + 2\mu \boldsymbol{S}), \quad \forall \boldsymbol{x} \in V_L. \tag{2.1b}$$

Here t is time, $\boldsymbol{u}$ is the liquid velocity, p is the dynamic pressure, $\boldsymbol{S} = (1/2)\left[(\nabla \boldsymbol{u})^{\mathrm{T}} + \nabla \boldsymbol{u}\right]$ is the rate of strain tensor, $\mu = \rho \nu$ is the liquid viscosity, ν is the liquid kinematic viscosity, g is the gravitational acceleration, $\boldsymbol{e}_x$ is the unit vector in the x-direction and $\boldsymbol{\delta}$ is the unit tensor. The body force term $-\phi \rho g \boldsymbol{e_x}$ in (2.1b) is composed of gravity and hydrostatic pressure and is derived in the Appendix. In the present numerical method (2.1b), modified as described below, is solved over the entire domain covering both the liquid phase as well as the gas phase. Since the mass density inside the gas phase is different to that being used in (2.1b), the flow solution is considered physically meaningful only in the liquid phase.

The liquid flow field is subjected to periodic boundary conditions at the domain boundaries and free-slip and no-penetration boundary conditions on the moving, spherical bubbles. Denoting the surface of the bubble by S and the bubble velocity by $\boldsymbol{u}_B$, the no-penetration condition is written as

$$(\boldsymbol{u} - \boldsymbol{u}_B) \cdot \boldsymbol{n} = 0 \quad \forall \boldsymbol{x} \in S, \tag{2.2}$$

and the zero tangential stress condition is written as

$$2\mu \boldsymbol{S} \cdot \boldsymbol{n} \cdot (\boldsymbol{\delta} - \boldsymbol{nn}) = \boldsymbol{0}. \quad \forall \boldsymbol{x} \in S. \tag{2.3}$$

Here $\boldsymbol{n}$ is the unit outward normal vector on S. The no-penetration and the zero tangential stress conditions are enforced by adding a force field $\boldsymbol{F}$ and a stress field $\boldsymbol{\sigma}$ to the right-hand side of (2.1b). This approach is an extension of the method of Uhlmann (2005). This immersed boundary method involves interpolations from the Eulerian grid that is used to compute the fluid field onto a Lagrangian grid that is used to describe the particle surface. Although physically irrelevant, information from the inside of the particle is used to perform the interpolations. This is a well-established method for enforcing boundary conditions on solid particles, which has previously been used to simulate turbulent flows of particle suspensions (Uhlmann 2008; Lucci, Ferrante & Elghobashi 2010).

In addition to adding $\boldsymbol{F}$ and $\boldsymbol{\sigma}$ to (2.1b), we also modify the body force term in (2.1b) to ensure that the gas bubbles experience the correct buoyancy force. Therefore, $\forall \boldsymbol{x} \in V_G$ the term $-\phi\rho g \boldsymbol{e_x}$ is replaced by $(1-\phi)\,\rho g \boldsymbol{e_x}$. The resulting equation of fluid motion therefore reads

$$\rho\left(\frac{\partial \boldsymbol{u}}{\partial t} + \boldsymbol{u}\cdot\nabla\boldsymbol{u}\right) = (G_L\Psi(\boldsymbol{x}) + G_G\,[1-\Psi(\boldsymbol{x})])\,\boldsymbol{e_x} + \boldsymbol{F} + \nabla\cdot(-p\boldsymbol{\delta} + 2\mu\boldsymbol{S} + \boldsymbol{\sigma}), \tag{2.4a}$$

where G_L and G_G are body forces due to gravity and hydrostatic pressure in the liquid phase and the gas phase,

$$G_L = -\phi\rho g, \quad G_G = (1-\phi)\,\rho g, \tag{2.4b}$$

and Ψ is a marker function being 0 inside the gas phase and 1 inside the liquid phase.

The fluid equation of motion (2.4) is discretized on a cubic and homogeneous mesh. The locations of the grid points are given by: $\boldsymbol{x}_{i,j,k} = \Delta x\left(i\boldsymbol{e}_x + j\boldsymbol{e}_y + k\boldsymbol{e}_z\right)$, where Δx is the grid spacing and i, j and k are integers. The domain sizes and number of grid points in the x, y and z direction are denoted (L_x, L_y, L_z) and (N_x, N_y, N_z), respectively.

2.2. *Boundary conditions*

2.2.1. *No-penetration*

The no-penetration condition (2.2) is enforced by the addition of the force field $\boldsymbol{F}$ to (2.4a). This force field is localized around the bubble surface S and has a direction normal to the bubble surface $\boldsymbol{n}$. The force $\boldsymbol{F}$ is defined such that it drives the normal component of the fluid velocity $\boldsymbol{u}$ at the bubble surface to the normal component of the bubble velocity $\boldsymbol{u}_B$. The force field is constructed by means of a set of N control points which are distributed equidistantly over S. The fluid velocity on these control points is interpolated from the values at the grid points. On each control point, a force is computed that counteracts the normal component of the difference

between the interpolated fluid velocity and $\boldsymbol{u}_B$. This force is then distributed to the neighbouring grid points using the following weights:

$$K(\boldsymbol{x}-\boldsymbol{y}) = \prod_{i=1}^{3} \delta\left(\frac{x_i - y_i}{\Delta x}\right). \tag{2.5a}$$

Here $\boldsymbol{y}$ is the location of the control point, $\boldsymbol{x}$ is the location of a grid cell and $\delta(x)$ is a regularized delta-function, which is smoothed over three grid cells Δx (Roma, Peskin & Berger 1999; Uhlmann 2005),

$$\delta(x) = \begin{cases} \frac{1}{3}(1+\sqrt{-3x^2+1}), & \text{if } |x| < \frac{1}{2}, \\ \frac{1}{6}(5-3x-\sqrt{-3(1-x)^2+1}), & \text{if } \frac{1}{2} < |x| < \frac{3}{2}, \\ 0, & \text{if } \frac{3}{2} < |x|. \end{cases} \tag{2.5b}$$

In contrast to the weights corresponding to Lagrangian interpolation, these weights provide a smooth temporal variation of the hydrodynamic forces while the bubble moves continuously with respect to the fixed Eulerian grid.

The no-penetration force, due to a single control point at position $\boldsymbol{y}_\alpha$ takes the form of a smoothed delta function, which is centred around $\boldsymbol{y}_\alpha$, and whose strength is proportional to $(\boldsymbol{u}_\alpha - \boldsymbol{u}_B)\cdot\boldsymbol{n}_\alpha$. Here $\boldsymbol{u}_\alpha$ and $\boldsymbol{n}_\alpha$ are the fluid velocity and bubble normal at control point α. Taking all N control points on S into account, the no-penetration force field $\boldsymbol{F}$ reads

$$\boldsymbol{F}(\boldsymbol{x}) = \sum_{\alpha=1}^{N} \boldsymbol{F}_\alpha K(\boldsymbol{x}-\boldsymbol{y}_\alpha), \tag{2.6a}$$

where

$$\boldsymbol{F}_\alpha = \frac{\rho \Delta S}{\Delta t \Delta x^2}(\boldsymbol{u_B} - \boldsymbol{u}_\alpha)\cdot\boldsymbol{n}_\alpha\boldsymbol{n}_\alpha. \tag{2.6b}$$

Here ΔS is the surface area corresponding to a single control point $\Delta S = 4\pi R^2/N$. We used $\Delta S = 0.5\Delta x^2$, since smaller values did not improve the accuracy of the method. The kernel given by (2.5) is also used to perform the interpolation. For a field u, the value u_α on point $\boldsymbol{y}_\alpha$ is interpolated from the values at the grid points $u_{i,j,k}$ as follows:

$$u_\alpha = \sum_{i=1}^{N_x}\sum_{j=1}^{N_y}\sum_{k=1}^{N_z} K(\boldsymbol{x}_{i,j,k}-\boldsymbol{y}_\alpha)u_{i,j,k}. \tag{2.7}$$

2.2.2. *Zero tangential stress*

In addition to no-penetration, free-slip on the bubble surface also requires zero tangential stress (2.3). This condition is satisfied by adding the stress field $\boldsymbol{\sigma}$ to (2.4*a*). Similar to the no-penetration force field $\boldsymbol{F}$, this tangential stress field $\boldsymbol{\sigma}$ is non-zero only in the vicinity of the bubble surfaces. The stress field counterbalances the shear components of $2\mu\boldsymbol{S}$ on the bubble surfaces. The procedure of computing $\boldsymbol{\sigma}$ is analogous to that of $\boldsymbol{F}$, involving the control points on the bubble surface. On each control point, the shear components of $2\mu\boldsymbol{S}$ with respect to the bubble tangent plane are computed, using the interpolation scheme given in (2.7). The stress tensor $\boldsymbol{\sigma}'$ that counterbalances these components is distributed to the neighbouring grid nodes using the weights given in (2.5). In this procedure, we identify at each control point the shear components of $2\mu\boldsymbol{S}$ with respect to the bubble tangent plane. For this purpose,

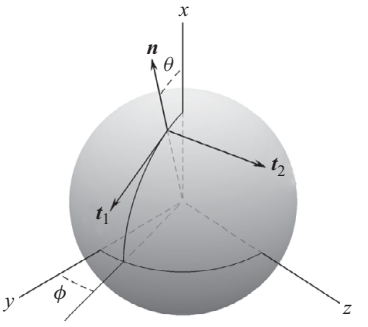

FIGURE 2. Sketch of the bubble normal unit vector $\boldsymbol{n}$ and the bubble tangent unit vectors $\boldsymbol{t_1}$ and $\boldsymbol{t_2}$ at spherical coordinates θ and ϕ.

we define at each control point an orthogonal coordinate system spanned by the unit normal $\boldsymbol{n}$ and two unit tangents $\boldsymbol{t}_1$ and $\boldsymbol{t}_2$. A sketch of this system is provided in figure 2. Using spherical coordinates (θ, ϕ), the transformation matrix between the $(\boldsymbol{e}_x, \boldsymbol{e}_y, \boldsymbol{e}_z)$-frame and the $(\boldsymbol{n}, \boldsymbol{t}_1, \boldsymbol{t}_2)$-frame reads

$$\boldsymbol{M} = \begin{pmatrix} \cos\theta & -\sin\theta & 0 \\ \sin\theta\cos\phi & \cos\theta\cos\phi & -\sin\phi \\ \sin\theta\sin\phi & \cos\theta\sin\phi & \cos\phi \end{pmatrix}. \tag{2.8}$$

We construct a tensor $\boldsymbol{\sigma}'$ that when added to $2\mu\boldsymbol{S}$ produces zero viscous shear stress with respect to the tangent plane of the sphere, without affecting the normal stress components. In the $(\boldsymbol{n}, \boldsymbol{t}_1, \boldsymbol{t}_2)$-frame, the 12, 21, 13 and 31 components correspond to this shear stress. Therefore, in the $(\boldsymbol{n}, \boldsymbol{t}_1, \boldsymbol{t}_2)$-frame, the 12, 21, 13 and 31 components of $\boldsymbol{\sigma}'$ are given opposite values as those of $2\mu\boldsymbol{S}$, while all others are set to be zero. In the $(\boldsymbol{e}_x, \boldsymbol{e}_y, \boldsymbol{e}_z)$-frame, this tensor is written as

$$\sigma'_{ij} = -2\mu_{ijkl}S_{kl}, \tag{2.9a}$$

where the fourth-order viscosity tensor equals

$$\mu_{ijkl} = \mu(M_{i1}M_{j2}M_{1k}M_{2l} + M_{i2}M_{j1}M_{2k}M_{1l} + M_{i1}M_{j3}M_{1k}M_{3l} + M_{i3}M_{j1}M_{3k}M_{1l}). \tag{2.9b}$$

Adding $\boldsymbol{\sigma}'$ to $2\mu\boldsymbol{S}$ satisfies zero tangential stress at a single point. Taking all control points on the surface into account, the tangential stress field is written as

$$\boldsymbol{\sigma}(\boldsymbol{x}) = \frac{\Delta S}{\Delta x^2}\sum_{\alpha=1}^{N}\boldsymbol{\sigma}'_\alpha K(\boldsymbol{x} - \boldsymbol{y}_\alpha), \tag{2.10}$$

where $\boldsymbol{\sigma}'_\alpha$ correspond to $\boldsymbol{\sigma}'$ (2.9) at control point α.

2.2.3. *Bubble motion*

The numerical integration of Newton's second law for a bubble, having a small mass, requires a small time step. In order to maintain the computational efficiency of the present numerical method, we circumvent this problem by assuming a zero bubble mass, which eliminates the acceleration term from the equation of bubble motion. Without the acceleration term, the equation of bubble motion (A 11) states that the hydrodynamic forces integrate to zero over the bubble surface. In addition to the

hydrodynamic forces, the simulated gas bubble also experiences a contribution from the force field $\boldsymbol{F}(\boldsymbol{x})$ (2.6), which is introduced to satisfy the no-penetration condition. The contribution of the artificial force field $\boldsymbol{F}$ can be minimized by equating its total sum to zero,

$$\sum_{\alpha=1}^{N} \boldsymbol{F}_\alpha = \boldsymbol{0}, \tag{2.11}$$

where $\boldsymbol{F}_\alpha$ is defined in (2.6*b*). Combining (2.6*b*) and (2.11) gives the following equation of bubble motion:

$$\sum_{\alpha=1}^{N} (\boldsymbol{u}_B - \boldsymbol{u}_\alpha) \cdot \boldsymbol{n}_\alpha \boldsymbol{n}_\alpha = \boldsymbol{0}. \tag{2.12}$$

By approximating $\sum_{\alpha=1}^{N} \boldsymbol{n}_\alpha \boldsymbol{n}_\alpha = N\boldsymbol{\delta}/3$, we arrive at the following expression for the bubble velocity:

$$\boldsymbol{u}_B = \frac{3}{N} \sum_{\alpha=1}^{N} \boldsymbol{u}_\alpha \cdot \boldsymbol{n}_\alpha \boldsymbol{n}_\alpha. \tag{2.13}$$

It is noted that the model can be easily extended to account for non-zero bubble mass by incorporating an inertia term into (2.13).

2.3. *Lattice Boltzmann method*

To approximate the solution to (2.4), we use our in-house lattice Boltzmann (LB) code (Ten Cate *et al.* 2004). The LB method is based on discretizing the Boltzmann equation, which governs the distribution function f over the space of the molecular velocity $\boldsymbol{v}$ and position $\boldsymbol{x}$ (Cercignani 1988),

$$\frac{\partial f}{\partial t} + \boldsymbol{v} \cdot \nabla f + \boldsymbol{a} \cdot \nabla_{\boldsymbol{v}} f = \frac{f^{(0)} - f}{\tau}. \tag{2.14a}$$

Here $\nabla_{\boldsymbol{v}}$ is the nabla operator in velocity space, and $\boldsymbol{a}$ is the acceleration due to gravity, mean pressure gradient and the no-penetration force field,

$$\boldsymbol{a} = g\boldsymbol{e}_{\boldsymbol{x}} \{-\phi \Psi(\boldsymbol{x}) + (1-\phi)[1 - \Psi(\boldsymbol{x})]\} + \boldsymbol{F}/\rho. \tag{2.14b}$$

The right-hand side of (2.14*a*) is the BGK approximation for the redistribution of probability due to molecular collisions, which is modelled as a relaxation process towards the Maxwell Boltzmann distribution $f^{(0)}$ corresponding to maximum entropy (Bhatnagar, Gross & Krook 1954).

The key of the LB method is to discretize the velocity space into a minimum set of velocities $\boldsymbol{v}_\alpha$, that is still large enough to represent the essential features of f that play a role in the Navier–Stokes limit. Therefore, the set $\boldsymbol{v}_\alpha$ is chosen such that it facilitates a spectral representation of f in Hermitian basis functions up to second order by using the Gauss–Hermite quadrature (He & Luo 1997; Philippi *et al.* 2006). The Hermite polynomials play a special role, since it can be shown that the corresponding expansion coefficients g_α are identical to the microscopic velocity moments of the distribution function, which represent the macroscopic flow quantities. Since the velocity directions $\boldsymbol{v}_\alpha$ are such that $\Delta t \boldsymbol{v}_\alpha$ equal the distances between neighbouring lattice points, the Lagrangian derivative in (2.14*a*) is numerically integrated over one time step Δt by simply shifting f_α between neighbouring lattice points, where f_α equals f evaluated at $\boldsymbol{v}_\alpha$, multiplied with the corresponding weight of the Gauss–Hermite quadrature.

$R/\Delta x$	$L_x/\Delta x$	Re	C_D	$\dfrac{C_D - C_{D,0}}{C_{D,0}}$	Δ/δ_V
4.5	48	4.92	4.48	0.02	0.35
4.5	48	16.9	1.42	−0.13	0.64
4.5	48	56.3	0.53	−0.13	1.2
6	64	53.6	0.59	−0.08	0.86
9	96	50.8	0.64	−0.04	0.56
12	128	50.4	0.67	−0.008	0.42
9	96	140	0.300	0.08	1.4
12	128	436	0.114	0.16	1.2

TABLE 1. Parameters and numerical results for steady, individual bubble rise. The domain dimensions are $L_x = 2L_y = 2L_z$, the time step is $\Delta t U_{slip}/\Delta x = 0.05$, the $C_{D,0}$ corresponds to a correlation from the literature (1.4), $\delta_V = R\sqrt{2/Re}$ is the boundary layer thickness.

In the present LB method, the acceleration $\boldsymbol{a}\cdot\nabla_{\boldsymbol{v}} f$ and the collision operator $(f^{(0)} - f)/\tau$ in (2.14) are applied in the space spanned by the hydrodynamical moments g_α which are linear combinations of f_α. These moments represent the mass density ρ, the components of the momentum density $\rho\boldsymbol{u}$ and the components of the momentum flux $\rho\boldsymbol{uu} - 2\mu\boldsymbol{S} - \boldsymbol{\sigma}$. With the present set of 18 discrete velocities, only moments up to second order can be accurately calculated and therefore the third- and higher-order moments have no physical significance in the present numerical method. It is noted that these higher order moments can be incorporated by extending the set of discrete velocities, which then lead to higher-order approximations of the Boltzmann equation describing fluid mechanics beyond the Navier–Stokes equations (Shan, Yuan & Chen 2006; Colosqui 2010). In the present method, the acceleration and the collision operator are applied in g_α-space, by adding $\Delta t\rho\boldsymbol{a}$ to the momentum density and adding $(4/3)\rho c_s^2\Delta t\boldsymbol{S}$ to the momentum flux, where c_s is the speed of sound which in the present LB method equals $c_s = \Delta x/(\sqrt{2}\Delta t)$. The spurious higher-order components are relaxed towards zero. Further details of this LB method can be found in Somers (1993).

The combination of the LB and the immersed boundary methods provides several advantages over conventional Navier–Stokes solvers. Firstly, the method provides a direct control over the hydrodynamic stresses. This property allows the use of a very efficient algorithm to drive the shear stresses on the bubble to zero. Secondly, all the hydrodynamic quantities are defined on the same grid, which provides more accuracy when performing the velocity and stress interpolations. Thirdly, since the LB method permits a small compressibility to the fluid, there is no need for a Poisson solver. In incompressible flow simulations, the Poisson solver alters the immersed boundary force field. The costly operations needed to negate the corresponding errors in the boundary conditions (Kim, Kim & Choi 2001) do not have to be applied when using the LB method.

2.4. *Single bubble*

In this section, we verify the accuracy of this method for the case of a single, steadily rising, spherical gas bubble by comparing the drag coefficient to a correlation from the literature (1.4). Results of these test cases are presented in table 1, showing the computed C_D and the corresponding difference to (1.4) for different grid resolutions and Reynolds numbers.

When simulating single bubble rise in a periodic domain, the size of the domain should be chosen to be sufficiently large, so that the hydrodynamic interaction between the bubble and its periodic images can be ignored. The dominant interaction is due to the wake produced by its upstream image, whose strength increases with increasing Reynolds number. Reducing these effects requires a rather large domain size in the x-direction corresponding to a large number of computational grid cells. In the single bubble simulations, we have alleviated these computational loads by changing the boundary conditions in the x-direction from periodic to inflow and outflow, thereby excluding the wake of the periodic upstream image. The inflow and the outflow conditions correspond to a uniform velocity on the $(x = x_B + L_x/2)$-plane, and zero derivatives in x of all hydrodynamic quantities on the $(x = x_B - L_x/2)$-plane, where x_B is the x-coordinate of the bubble centre. Being determined by x_B, the inflow and outflow planes move periodically in the x-direction. It is noted that the inflow and outflow conditions are only applied in the single bubble simulations. They are not applied in the bubble swarm simulations of § 3. Using these conditions in the x-direction and using periodic boundary conditions in the y- and z-directions, the model predicts a C_D within 10 % of the literature value, using domain sizes of $L_x/R \approx 10$ and $L_y/R = L_z/R \approx 5$. For smaller domain sizes, the drag coefficient is generally predicted to be larger.

In addition to the domain size, the second parameter that determines the accuracy of the numerical result is the grid resolution. Obtaining an accurate numerical solution requires that the grid spacing Δx is smaller than the viscous boundary layer thickness $\delta_V = R\sqrt{2/Re}$ (Blanco & Magnaudet 1995). In the present work, we study bubble swarms at large Reynolds numbers up to $Re \approx 2000$. In order to keep the computational loads within feasible limits, we have used $\Delta x \approx \delta_V$, which corresponds to $R/\Delta x = 12$ for $Re = 500$ and $R/\Delta x = 24$ for $Re = 2000$. Although this resolution is somewhat too coarse to fully resolve the velocity profile inside the viscous boundary layer, the C_D results for single bubble rise are reasonable. As shown in table 1, this resolution yields a drag coefficient within 15 % of the literature value for $Re \approx 56$, 140 and 440. For smaller Reynolds numbers $Re \lesssim 20$, however, a resolution of $\Delta x \approx \delta_V$, yields a too small value for $R/\Delta x$, such that the spherical object can no longer be represented accurately in the grid. We found that for $Re \lesssim 20$ a minimum of $R/\Delta x = 4.5$ must be used to obtain a C_D within 15 % of the literature value. This minimum of $R/\Delta x = 4.5$ is related to the immersed boundary method, which effectively smears out the gas–liquid interface over three grid nodes. Apparently the bubble diameter must be at least a few times as large as this thickness in order to obtain reasonable results.

In table 1, we illustrate the grid dependence of the method for $Re \approx 50$. For this purpose, we show results for four simulations with increasing grid resolution, corresponding to $\Delta x/\delta_V = 1.2$, 0.9, 0.6 and 0.4. Table 1 shows that with increasing grid resolution C_D approaches the literature and reaches a value within 1 % of the literature value for $\Delta x/\delta_V = 0.4$.

In figure 3, we examine for these four cases the accuracy of the immersed boundary method to satisfy the free-slip boundary condition. In that figure, we show the penetration velocity u_r scaled with U_{slip} and the shear stress on the bubble $2\mu S_{r\theta} + \sigma_{r\theta}$ scaled with $C_D(1/2)\rho U_{slip}^2$. These variables are shown as functions of the spherical coordinate θ, which is defined in figure 2. From figure 3, we conclude that the no-penetration condition is satisfied within 2 % of the slip velocity and the zero tangential stress condition is satisfied within 0.5 % of the average stress on the bubble. These results are roughly independent

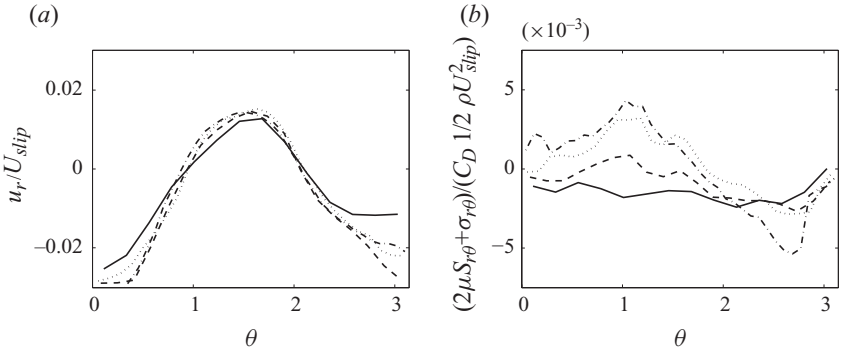

FIGURE 3. Penetration velocity (a) and shear stress (b) on the bubble surface for steady isolated bubble rise using $Re = 50$, $R/\Delta x = 4.5$ (solid line), $R/\Delta x = 6.0$ (dashed line), $R/\Delta x = 9.0$ (dotted line) and $R/\Delta x = 12.0$ (dash-dotted line). Additional numerical parameters are given in table 1.

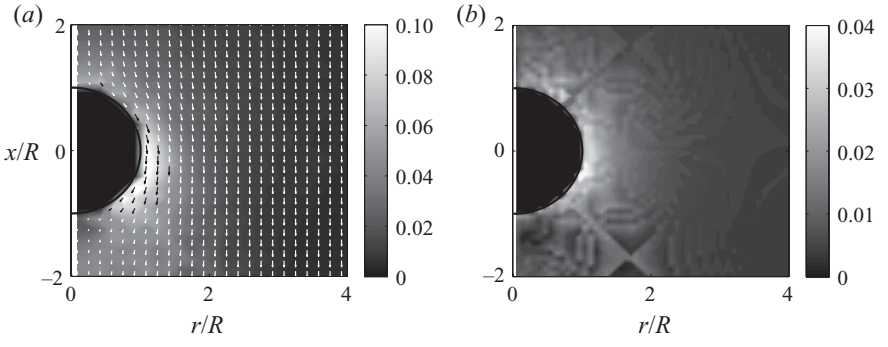

FIGURE 4. Simulation results of a single rising gas bubble. The grey scale indicates the velocity difference magnitude, in U_{slip}-units, between our method and the method of Mei & Klausner (1992). The results from our method are obtained using $Re = 10$, $L_x/R = 42\frac{2}{3}$, $L_y/L_x = L_z/L_x = 1/2$, $R/\Delta_x = 6$, $L_x/\Delta_x = 256$ (a) and $R/\Delta x = 12$, $L_x/\Delta x = 512$ (b). The vectors in the left figure correspond to the velocity field predicted by our method. We have set the vectors in the gas bubble to zero.

of grid resolution. With diminishing grid size, the shear stress is seen to increase slightly.

In figure 4, we examine the accuracy of the method to produce the correct velocity field around the bubble. For this purpose, we compare our result for $Re = 10$ to the finite difference result of Mei & Klausner (1992), who used a finite difference method on a spherical grid with a fine grid spacing in the radial direction close to the bubble surface. From figure 4, it is seen that the difference between our result and the result of Mei & Klausner (1992) is $\leqslant 0.1U_{slip}$ for $R/\Delta x = 6$ and $\leqslant 0.04U_{slip}$ for $R/\Delta x = 12$. The maximum difference occurs within one Δx of the bubble surface, due to the presence of the unphysical immersed boundary force and stress fields.

Finally it is noted that the numerical results are insensitive to the time step, provided that $\Delta t U_{slip}/\Delta x \lessapprox 0.1$.

N_B	$R/\Delta x$	$L_x/\Delta x$	ϕ	Re	C_D
64	4.5	96	0.027	5.1	4.9
256	4.5	96	0.110	5.0	5.9
1024	4.5	96	0.442	5.0	8.2
64	6	128	0.027	50	0.87
256	6	128	0.110	49	1.2
1024	6	128	0.442	49	2.0
64	12	256	0.027	532	0.26
256	12	256	0.110	508	0.51
1024	12	256	0.442	479	1.60
32	24	256	0.110	2084	0.64

TABLE 2. Parameters and numerical results of buoyancy-driven bubble suspensions. The time step is $\Delta t U_{slip}/\Delta x = 0.05$.

3. Bubble swarms

3.1. *Numerical parameters*

The principal aim of the present work is to study the relation between the drag coefficient C_D, the gas volume fraction ϕ and the bubble Reynolds number Re in buoyancy-driven suspensions of spherical gas bubbles. For this purpose, we have conducted 10 simulations using three values of the gas volume fraction $\phi \approx 0.028$, 0.11 and 0.44 and four values of the Reynolds number $Re \approx 5$, 50, 500 and 2000. All parameters are listed in table 2. For each simulation gravity is tuned iteratively such that Re reaches the desired value. In all simulations, $\Delta t U_{slip}/\Delta x \approx 0.05$ and the domain is cubical with linear dimensions $L_x/R = 21\frac{1}{3}$, except for the $Re = 2000$ case, where the domain size is $L_x/R = 10\frac{2}{3}$. For $Re \approx 5$, 50, 500 and 2000, we have used $R/\Delta x = 4.5$, 6, 12 and 24, respectively. The corresponding grid spacings Δx per viscous boundary layer thickness δ_V are $\Delta x/\delta_V \approx 0.4$, 0.9, 1.2 and 1.2, respectively. As discussed in § 2.4, a grid resolution of $\Delta x/\delta_V \approx 1$ is somewhat too coarse to fully resolve the velocity profiles within the viscous boundary layer. However for single bubble rise the associated errors were shown to be modest, with a drag coefficient within 15 % of the literature value. We have chosen to use this resolution, since it allows simulations of bubble swarms at large Reynolds numbers using reasonable amounts of computational resources. In this context, it is further noted that the error of 15 % is of minor concern compared to more fundamental inconsistencies between the simulations and real bubble swarms, such as the neglect of bubble deformation, bubble coalescence, bubble polydispersity, walls and impurities at the gas–liquid interface. These effects are expected to cause larger discrepancies between the simulations and experiments as compared to the 15 % error due to the slightly under-resolved viscous boundary layer.

After starting the simulation from a random distribution of bubbles, a transition period of $\sim 100 R/U_{slip}$ time units is required before the flow reaches a statistically steady state, after which statistics are collected during another $\sim 100 R/U_{slip}$ time units.

3.2. *Microstructure*

Figure 1 shows the y-component of the liquid velocity vector in the xz-plane at $\phi \approx 0.11$ for the four different Reynolds numbers considered $Re \approx 5$, 50, 500 and 2000. The circles in the figure indicate the cross-sections of the bubbles with the plane. As can be seen from these plots, the structure of the flow is markedly different for $Re \approx 5$ and $Re \approx 50$ as compared to $Re \approx 500$ and $Re \approx 2000$. The larger Re cases

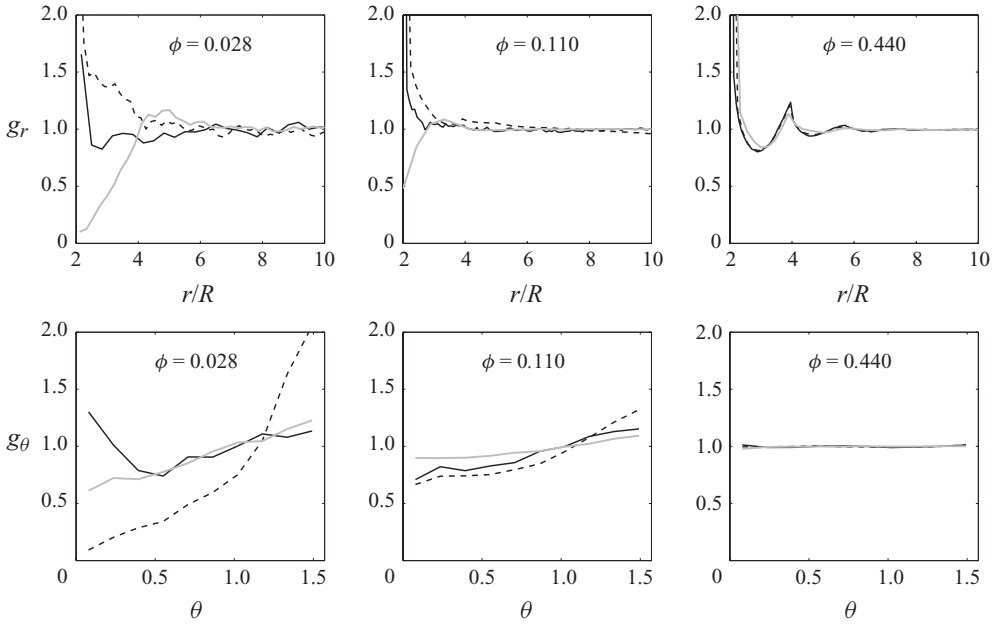

FIGURE 5. Radial pair distribution $g_r(r)$ and polar pair distribution $g_\theta(\theta)$ for $Re \approx 5$ (grey lines), $Re \approx 50$ (dashed black lines) and $Re \approx 500$ (solid black lines).

exhibit fluid velocity fluctuations on scales smaller than the bubble radius, which are absent for the smaller Re cases. We will, therefore, refer to flow as 'high agitation' for $Re \gtrsim 100$, and we use 'low agitation' to refer to the flow for $Re \lesssim 100$.

By inspecting the bubble positions from plots such as those in figure 1, we verified that the bubbles were dispersed homogeneously for all cases. Although bubbles tend to form pairs, there was no sign of large-scale structuring into horizontal planes, such as observed in the potential flow simulations of Sangani & Didwania (1993), nor into vertical drafts, such as observed in the DNS of flexible bubbles of Bunner & Tryggvason (2003). To study the relative positioning of the bubbles, we have computed the bubble pair probability density function $g(\boldsymbol{r})$. This function is defined such that $g(\boldsymbol{r})\mathrm{d}\boldsymbol{r}$ is proportional to the probability of finding a bubble pair whose separation vector lies within a volume $\mathrm{d}\boldsymbol{r}$ around $\boldsymbol{r}$. The function $g(\boldsymbol{r})$ is normalized such that $g = 1$ corresponds to a random distribution of bubbles. The separation vector $\boldsymbol{r}$ is parameterized using spherical coordinates (r, θ), where r is the length of $\boldsymbol{r}$ and θ is the angle from the x-axis to $\boldsymbol{r}$. We have computed $g(r, \theta)$ for $2 < r/R < 10$ by using bin sizes of $\Delta r = \Delta x$ and $\Delta\theta = \pi/20$.

Figure 5 shows the radial pair distribution which is defined as

$$g_r(r) = \frac{\displaystyle\int_{r-\Delta r/2}^{r+\Delta r/2}\int_0^{\pi}\left[\mathrm{d}\tilde{\theta}\,\sin\tilde{\theta}\,\mathrm{d}\tilde{r}\tilde{r}^2 g(\tilde{r},\tilde{\theta})\right]}{2r^2\Delta r}. \tag{3.1}$$

For the small volume fraction $\phi = 0.028$, there is a clear Re-dependence of the microstructre. For $Re \approx 5$ bubbles do not come close together, reflected by small $g_r(r/R < 4)$. The opposite holds for $Re \approx 50$ and 500 where a large peak is seen at $r/R = 2$ corresponding to direct bubble contacts. For the intermediate volume fraction $\phi = 0.11$, the trends are similar as for $\phi = 0.028$, but the density variations

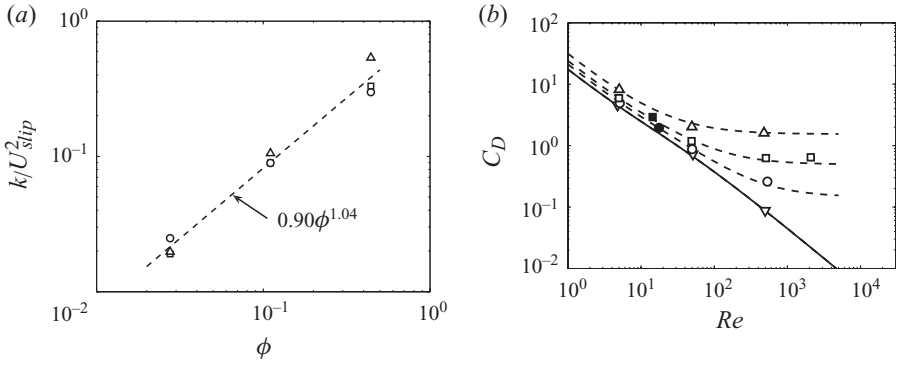

FIGURE 6. (*a*) Kinetic energy of the fluid velocity fluctuations, $k = \frac{1}{2}\overline{\boldsymbol{u}' \cdot \boldsymbol{u}'}$, versus gas volume fraction ϕ for Reynolds number $Re \approx 5$ (circles), $Re \approx 50$ (squares) and $Re \approx 500$ (triangles). The dashed line shows the least-square, power-law fit. (*b*) Drag coefficient C_D as a function of the Reynolds number Re for gas volume fractions of $\phi = 0.0$ (single bubble, downward triangles), $\phi \approx 0.028$ (circles), $\phi \approx 0.11$ (squares) and $\phi \approx 0.44$ (upward triangles). The solid line is a correlation from the literature for the rise of a single spherical bubble (1.4). The dashed lines are predictions by our model (3.7). The white symbols correspond to the present simulations, the black symbols correspond to the simulations of Yin & Koch (2008).

are confined to smaller radial distances. For the large volume fraction $\phi = 0.44$, there is no apparent Reynolds number dependence in $g(r)$. The curves for all three Re cases collapse showing a large peak at $r/R = 2$ and a secondary peak at $r/R = 4$.

Figure 5 also shows the polar pair distribution which is defined as

$$g_\theta(\theta) = \frac{\displaystyle\int_{2R}^{5R}\int_{\theta-\Delta\theta/2}^{\theta+\Delta\theta/2} \left[\mathrm{d}\tilde{\theta}\sin\tilde{\theta}\,\mathrm{d}\tilde{r}\tilde{r}^2 g(\tilde{r},\tilde{\theta})\right]}{39R^3\sin\theta\,\Delta\theta}, \tag{3.2}$$

where we only consider bubbles which are close together $2 < r/R < 5$. Preferred horizontal alignment corresponds to large g_θ around $\theta = \pi/2$, while vertical alignment corresponds to large g_θ around $\theta = 0$. For $\phi = 0.028$ we find a strong Re-dependence in g_θ. For $Re \approx 5$ and 50 there is a modest and a strong preferred horizontal alignment, while for $Re \approx 500$ there is a preferred vertical alignment. For $\phi \approx 0.11$ all three Re cases show preferred horizontal alignment, which is strongest for $Re \approx 50$. For $\phi = 0.44$ the curves for all three Re cases collapse showing no significant preferred alignment angle.

Another interesting property of the microstructure is presented in figure 6(*a*), where we plot the scaled kinetic energy contained in the liquid velocity fluctuations: $k/U_{slip}^2 = \frac{1}{2}\overline{\boldsymbol{u}' \cdot \boldsymbol{u}'}/U_{slip}^2$. In agreement with previous experimental observations (Garnier, Lance & Marié 2002; Riboux, Risso & Legendre 2010), we find that this quantity scales linearly with ϕ while being roughly independent of Re. This similarity for different Re is striking, given the marked flow changes, as shown in figure 1. In the next section, we will exploit this similarity when formulating a model for the drag force in terms of an effective viscosity based on the stress carried by the velocity fluctuations in the liquid.

3.3. *Drag coefficient*

In figure 6(*b*), we plot the computed C_D as a function of Re. For clarity, we have included lines of constant $\phi = 0$, 0.028, 0.11 and 0.44 as predicted by our model (3.7) using $We = 0$. The model is derived below. To verify our numerical results, we

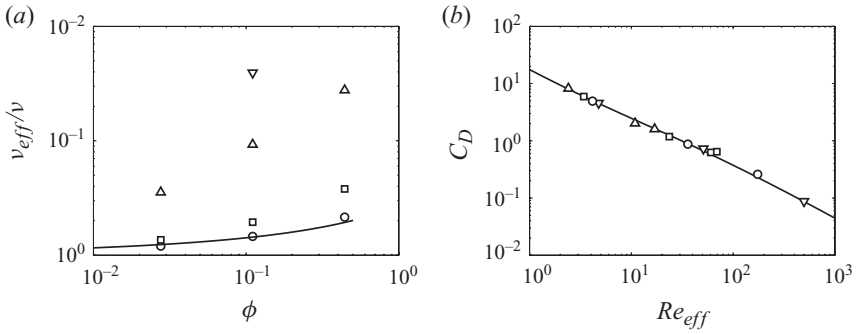

FIGURE 7. (*a*) Relative effective viscosity ν_{eff}/ν versus the gas volume fraction ϕ for Reynolds numbers of $Re \approx 5$ (circles), $Re \approx 50$ (squares), $Re \approx 500$ (upward triangles) and $Re \approx 2000$ (downward triangle). The solid line is a curve fit for the $Re \approx 5$ case (3.3). (*b*) Drag coefficient C_D as a function of the effective Reynolds number Re_{eff} (3.6) for gas volume fractions of $\phi = 0.0$ (single bubble, downward triangles), $\phi \approx 0.028$ (circles), $\phi \approx 0.11$ (squares) and $\phi \approx 0.44$ (upward triangles). The solid line is a correlation from the literature for the rise of a single spherical bubble (1.4).

also plot the results of Yin & Koch (2008), who used a lattice Boltzmann method to simulate buoyancy-driven rise of spherical bubble swarms, for $5 \lesssim Re \lesssim 20$ and $0 < \phi < 0.25$. To facilitate a proper comparison, we have interpolated the data of Yin & Koch (2008) to the same ϕ values as those used in the present simulations, i.e. $\phi = 0.028$ and 0.11. As can be seen in figure 6(*b*), there is a good match between the data of Yin & Koch (2008) and our model (3.7).

Figure 6(*b*) shows a transition. In the 'low agitation' regime ($Re \lesssim 100$), the lines of constant ϕ are shifted parallel with respect to the line for an individual bubble (1.4), while in the 'high agitation' regime ($Re \gtrsim 100$) the lines reach plateau values which are independent of Re. The observations made in § 3.2 that for $\phi = 0.44$ the $g(r, \theta)$ is Re-independent suggest that the differences in C_D between the 'low agitation' and the 'high agitation' regimes are not linked to differences in the microstructure. Conversely we will argue that the different regimes are due to the occurrence of small scale velocity fluctuations in the liquid phase, while changes in bubble cluster configurations are of minor importance.

In the following, we will develop a relation for C_D by assuming a similarity between the $C_D(Re_{eff})$ relation in the suspension and the $C_D(Re)$ relation of an individual bubble (1.4). Here the effective Reynolds number Re_{eff} is based on the effective viscosity ν_{eff} which is allowed to depend on the properties of the suspension. The concept of an effective viscosity has previously been used to capture the effect of hydrodynamic interactions on the drag force in suspensions (see for instance: Barnea & Mizrahi 1973; Ishii & Zuber 1979). To our knowledge, previous models always assumed that ν_{eff}/ν depends on ϕ only and is independent of Re. Here we will argue that for bubble swarms this assumption holds only for $Re \lesssim 100$. For $Re \gtrsim 100$, on the other hand, the occurrence of small scale velocity fluctuations introduces a Re dependence in ν_{eff}/ν. To demonstrate this, we have computed $\nu_{eff}/\nu = Re/Re_{eff}$ by inserting the simulated C_D values into (1.4), substituting Re_{eff} for Re and subsequently solving for Re_{eff}. The results are plotted in figure 7(*a*).

As expected the data for $Re \approx 5$ and 50, which correspond to the 'low agitation' regime, are relatively close to each other. We parametrize the 'low agitation' regime

by a curve-fit to the $Re \approx 5$ data,

$$\frac{\nu_{eff}}{\nu} = \frac{1}{1 - 0.6\phi^{1/3}}. \tag{3.3}$$

The form of this relation is similar to the analytical solution $\nu_{eff}/\nu = (1 - 1.1964\phi^{1/3} + 0.3508\phi^2)^{-1}$ for a fixed array of spherical gas bubbles in the creeping flow limit (Sangani & Acrivos 1983). For small ϕ (3.3) predicts: $\nu_{eff}/\nu = 1 + K\phi^{1/3}$, with K as a numerical constant. The term $\phi^{1/3} \sim R/D$ can be understood by considering its proportionality to the magnitude of a velocity disturbance carried over the distance D between two neighbouring bubbles (Barnea & Mizrahi 1973).

As opposed to the 'low agitation' regime figure 7(a) shows a clear Re-dependence of ν_{eff}/ν in the 'high agitation' regime. To construct a model that captures the physics in both regimes, we assume that the effective viscosity $\nu_{eff} = \nu_L + \nu_T$ is composed of a 'laminar' contribution ν_L as given by (3.3) and a 'turbulent' contribution ν_T. We define ν_T as the ratio of the stress carried by the velocity fluctuations: $k = (1/2)\overline{\boldsymbol{u}' \cdot \boldsymbol{u}'}$, and the typical shear rate U_{slip}/R,

$$\nu_{eff} = \nu_L + \nu_T = \frac{\nu}{1 - 0.6\phi^{1/3}} + \frac{CkR}{U_{slip}}, \tag{3.4}$$

where C is a constant of order unity. As shown in figure 6(a) and discussed in § 3.2, we use that: $k \approx U_{slip}^2\phi$. Inserting this into (3.4) gives the following relation for the effective viscosity ratio,

$$\frac{\nu_{eff}}{\nu} = \frac{1}{1 - 0.6\phi^{1/3}} + C\phi Re. \tag{3.5}$$

A value of 0.13 for C provides the best correlation between (3.5) and the simulation data. The difference between our relation (3.5) and earlier proposed relations is the Re dependence of ν_{eff}/ν. We argue that this dependence is essential to capture the effects of the small scale velocity fluctuations in the interstitial liquid, due to the randomly moving bubbles at large Re.

Figure 7(b) shows the simulation data on the (Re_{eff}, C_D) plane where the effective Reynolds number $Re_{eff} = 2RU_{slip}/\nu_{eff}$ is obtained from (3.5),

$$Re_{eff} = \frac{1}{\dfrac{1}{Re(1 - 0.6\phi^{1/3})} + 0.13\phi}. \tag{3.6}$$

The proposed model, which is plotted as the solid line, assumes that C_D is described by (1.4) where Re is replaced by Re_{eff}, which is given by (3.6). The validity of this approach is demonstrated by the collapse of the simulation data within 20 % of the solid line.

3.4. *Comparison to experimental data*

To summarize, we have derived a $C_D(Re, \phi)$ relation for spherical bubble swarms by assuming a similarity between the $C_D(Re_{eff})$ relation for the swarm and the $C_D(Re)$ relation for a single bubble (1.4). In the model, the effective Reynolds number Re_{eff} (3.6) is based on an effective viscosity which accounts for hindrance effects and turbulence effects. In order to extend our model to account for bubble deformation we hypothesize a similarity between the $C_D(Re_{eff}, We)$ relation in the suspension and the $C_D(Re, We)$-relation for a single bubble (1.6). We, therefore, propose the following

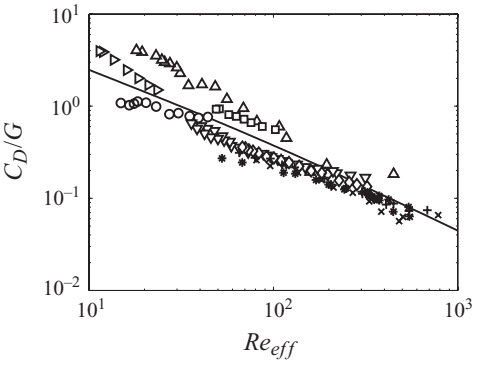

FIGURE 8. Drag coefficient C_D divided by distortion factor G (1.5) as a function of the effective Reynolds number Re_{eff} (3.6) for various experimental data on buoyancy-driven bubble suspensions. ○, $600 < Re < 750$, $0.15 < \phi < 0.5$, $1.3 < We < 1.6$, (Harteveld *et al.* 2003); △, $600 < Re < 900$, $0.07 < \phi < 0.4$, $0.8 < We < 2.4$, (Garnier *et al.* 2002); ▽, $300 < Re < 400$, $0.002 < \phi < 0.2$, $0.6 < We < 1.3$, (Zenit, Koch & Sangani 2001); ▷, $15 < Re < 25$, $0.004 < \phi < 0.06$, $0.1 < We < 0.2$, (Martínez-Mercado, Palacios-Morales & Zenit 2007); □, $80 < Re < 120$, $0.004 < \phi < 0.04$, $0.3 < We < 0.5$, (Martínez-Mercado *et al.* 2007); ◇, $400 < Re < 550$, $0.004 < \phi < 0.1$, $1.7 < We < 2.0$, (Martínez-Mercado *et al.* 2007); *, $400 < Re < 550$, $0.002 < \phi < 0.1$, $1.2 < We < 2.5$, (Riboux *et al.* 2010); +, $500 < Re < 700$, $0.002 < \phi < 0.1$, $2.7 < We < 3.2$, (Riboux *et al.* 2010); ×, $600 < Re < 800$, $0.003 < \phi < 0.07$, $2.1 < We < 3.5$, (Riboux *et al.* 2010). Our model is plotted as the line (3.7).

model for rising swarms of deformable bubbles:

$$\frac{C_D}{G} = \frac{16}{Re_{eff}} \left\{ 1 + \left[\frac{8}{Re_{eff}} + \frac{1}{2} \left(1 + 3.315 Re_{eff}^{-1/2} \right) \right]^{-1} \right\}, \tag{3.7}$$

where the distortion factor G and the effective Reynolds number Re_{eff} are defined in (1.5) and (3.6).

In order to determine the accuracy of this model, we compare it to experimental data from the literature. For this comparison, we use experimental (ϕ, U_{slip}, R) data, that have been obtained under homogeneous conditions, which means that no large scale circulation is present and that bubble coalescence and breakup do not play important roles. These conditions can be satisfied when bubbles are released in the column using carefully designed gas injection systems, that ensure a homogeneous distribution over the column cross-section and the bubbles are nearly monodisperse. We found nine experimental data sets from five different research groups, that were obtained under sufficiently well-controlled conditions to be suitable for the comparison. In figure 8, we plot these data on the (Re_{eff}, C_D/G) plane. The experimental conditions are summarized in the caption. The solid line in that figure represents our model (3.7). Given the uncertainties in the experiments and the simplifications in the simulations, the agreement is surprisingly good. The experimental data follow (3.7) within a factor of 3.

4. Conclusions

The complexity of bubbly flow at large Re lies in the combination of pseudo-turbulence and bubble deformation. To gain insight, we have reduced this complexity by ignoring bubble deformation and focusing on numerical simulations of spherical gas bubbles. These simulations were performed using a novel scheme based on lattice

Boltzmann and immersed boundary methods. This strategy has provided a clear picture of the effect of pseudo-turbulence on the drag force in bubble swarms. We found that these effects can be captured using an effective viscosity $\nu_{eff} \approx kR/U_{slip}$, where the liquid velocity fluctuations are observed to behave as $k \approx \phi U_{slip}^2$. To account for bubble deformation, we propose a modification of the model by using the distortion theory for a single gas bubble due to Moore (1965).

The principal assumption of our approach is a decoupling of the effects of the pseudo-turbulence from the effects of bubble deformation. Although the validity of this assumption is questionable, our approach resulted in a model that agrees reasonably well with experimental data from the literature. Furthermore, it has provided insights that are difficult to obtain from experiments where effects of turbulence and bubble deformation are interrelated in a complicated and yet unknown way. Therefore, we conclude that spherical bubble swarms provide a useful, limiting case in the analysis of deformable bubble swarms.

Appendix. Derivation of the hydrostatic pressure gradient, the bubble equation of motion and the drag coefficient

A.1. *Hydrostatic pressure gradient*

The flow in the liquid phase is described by the incompressible Navier–Stokes equation,

$$\rho\left(\frac{\partial \boldsymbol{u}}{\partial t} + \boldsymbol{u}\cdot\nabla\boldsymbol{u}\right) = -\left(\frac{\mathrm{d}P}{\mathrm{d}x} + \rho g\right)\boldsymbol{e_x} + \nabla\cdot(-p\boldsymbol{\delta} + 2\mu\boldsymbol{S}), \quad \forall \boldsymbol{x} \in V_L. \tag{A 1}$$

Pressure is partitioned into two terms. The hydrostatic pressure P varies linearly in the x-direction and the fluctuating pressure p varies periodically. The hydrostatic pressure gradient $\mathrm{d}P/\mathrm{d}x$ counteracts gravity such that conservation of overall momentum is guaranteed. An expression for $\mathrm{d}P/\mathrm{d}x$ can be obtained by averaging the x-component of (A 1) over the liquid phase. The averaging operator $\overline{\cdots}$ acts on a variable u in the following way:

$$\overline{u} = \frac{1}{V(1-\phi)}\int_V \Psi(\boldsymbol{x})u(\boldsymbol{x})\,\mathrm{d}V. \tag{A 2}$$

Here Ψ is a marker function being 0 inside the gas phase and 1 inside the liquid phase.

The flow is assumed statistically steady and V is assumed large enough that volume averages of hydrodynamic quantities are time independent. If we also use that all flow variables are periodic, we arrive at the following expression for the x-component of the volume-averaged Navier–Stokes equation:

$$0 = -(1-\phi)\left(\frac{\mathrm{d}P}{\mathrm{d}x} + \rho g\right) + I_x. \tag{A 3}$$

Here I_x is the x-component of the momentum transfer per unit volume from the gas phase to the liquid phase due to viscous and fluctuating pressure forces,

$$I_x = \frac{1}{V}\sum_{j=1}^{N_B}\int_{S_j}(p\boldsymbol{\delta} - 2\mu\boldsymbol{S}) : \boldsymbol{nnn}\cdot\boldsymbol{e_x}\,\mathrm{d}S. \tag{A 4}$$

Here $\boldsymbol{n}$ is the outward-pointing normal on the bubble surface. Only normal stress components contribute to I_x, since tangential components are identically zero

according to the free-slip boundary condition. The integral in (A 4) is taken over all bubble surfaces S_j. Assuming zero bubble mass, the total force acting on the bubbles equals zero,

$$\mathbf{0} = -\frac{1}{V}\sum_{j=1}^{N_B}\int_{S_j}(P\boldsymbol{\delta} + p\boldsymbol{\delta} - 2\mu\boldsymbol{S}) : \boldsymbol{nnn}\,\mathrm{d}S. \tag{A 5}$$

Applying Gauss' theorem to the P-term and using (A 4) gives the following force balance for the gas phase:

$$0 = -\phi\frac{\mathrm{d}P}{\mathrm{d}x} - I_x. \tag{A 6}$$

Using (A 6) to eliminate the interaction force I_x in (A 3) gives the following expression for the mean pressure gradient:

$$\frac{\mathrm{d}P}{\mathrm{d}x} = -(1-\phi)\,\rho g. \tag{A 7}$$

Combining (A 6) and (A 7) gives the following expression for the interaction force:

$$I_x = \phi\,(1-\phi)\,\rho g. \tag{A 8}$$

Inserting (A 7) into (A 1) gives the following equation for the liquid momentum:

$$\rho\left(\frac{\partial \boldsymbol{u}}{\partial t} + \boldsymbol{u}\cdot\nabla\boldsymbol{u}\right) = -\phi\rho g\boldsymbol{e_x} + \nabla\cdot(-p\boldsymbol{\delta} + 2\mu\boldsymbol{S}), \quad \forall \boldsymbol{x} \in V_L. \tag{A 9}$$

A.2. *Bubble motion*

Assuming zero bubble mass, the bubbles move such that the hydrodynamic forces integrate to zero over the bubble surface:

$$\mathbf{0} = -\int_S (P\boldsymbol{\delta} + p\boldsymbol{\delta} - 2\mu\boldsymbol{S}) : \boldsymbol{nnn}\,\mathrm{d}S. \tag{A 10}$$

Applying Gauss' theorem to the P-term and using (A 7) give the following equation of bubble motion:

$$\mathbf{0} = (1-\phi)\,\rho g V_B \boldsymbol{e}_x - \int_S (p\boldsymbol{\delta} - 2\mu\boldsymbol{S}) : \boldsymbol{nnn}\,\mathrm{d}S, \tag{A 11}$$

where V_B is the bubble volume.

A.3. *Drag coefficient*

The drag coefficient is defined as the interaction force per bubble,

$$C_D = \frac{I_x V}{N_B \pi R^2 \frac{1}{2}\rho U_{slip}^2}. \tag{A 12}$$

Inserting the expression (A 8) for I_x into (A 12) yields the following expression for C_D:

$$C_D = \frac{\frac{4}{3}R\,(1-\phi)\,g}{U_{slip}^2}. \tag{A 13}$$

REFERENCES

Barnea, E. & Mizrahi, J. 1973 A generalized approach to the fluid dynamics of particulate systems: Part 1. general correlation for fluidization and sedimentation in solid multiparticle systems. *Chem. Engng J.* **5**, 171–189.

Bhatnagar, P. L., Gross, E. P. & Krook, M. 1954 A model for collision processes in gases. *Phys. Rev.* **94**, 511.

Blanco, A. & Magnaudet, J. 1995 The structure of the axisymmetric high-Reynolds number flow around an ellipsoidal bubble of fixed shape. *Phys. Fluids* **7**, 1265.

Bunner, B. & Tryggvason, G. 2003 Effect of bubble deformation on the properties of bubbly flows. *J. Fluid Mech.* **495**, 77–118.

Cercignani, C. 1988 *The Boltzmann Equation and its Applications*. Springer.

Chen, M., Kontomaris, K. & McLaughlin, J. B. 1998 Direct numerical simulation of droplet collisions in a turbulent channel flow. Part I: collision algorithm. *Intl J. Multiphase Flow* **24**, 1079–1103.

Colosqui, C. E. 2010 High-order hydrodynamics via lattice Boltzmann methods. *Phys. Rev.* E **81**, 026702.

Duineveld, P. C. 1995 The rise velocity and shape of bubbles in pure water at high Reynolds number. *J. Fluid Mech.* **292**, 325–332.

Esmaeeli, A. & Tryggvason, G. 2005 A direct numerical simulation study of the buoyant rise of bubbles at $O(100)$ Reynolds number. *Phys. Fluids* **17**, 093303.

Garnier, C., Lance, M. & Marié, J. L. 2002 Measurement of local flow characteristics in buoyancy-driven bubbly flow at high void fraction. *Exp. Therm. Fluid Sci.* **26**, 811–815.

Harteveld, W. K., Mudde, R. F. & Van Den Akker, H. E. A. 2003 Dynamics of a bubble column: Influence of gas distribution on coherent structures. *Can. J. Chem. Engng* **81**, 389–394.

He, X. & Luo, L.-S. 1997 A priori derivation of the lattice Boltzmann equation. *Phys. Rev.* E **55** (6/A), 6333–6336.

Ishii, M. & Zuber, N. 1979 Drag coefficient and relative velocity in bubbly, droplet or particulate flows. *AIChE J.* **25**, 843–855.

Kim, J., Kim, D. & Choi, H. 2001 An immersed-boundary finite-volume method for simulations of flow in complex geometries. *J. Comput Phys.* **171**, 132–150.

Lucci, F., Ferrante, A. & Elghobashi, S. 2010 Modulation of isotropic turbulence by particles of Taylor length-scale size. *J. Fluid Mech.* **650**, 5–55.

Martínez-Mercado, J., Palacios-Morales, C. A. & Zenit, R. 2007 Measurement of pseudoturbulence intensity in monodispersed bubbly liquids for $10 < \mathrm{Re} < 500$. *Phys. Fluids* **19**, 103302.

Maxworthy, T., Gnann, C., Kurten, M. & Durst, F. 1996 Experiments on the rise of air bubbles in clean viscous liquids. *J. Fluid Mech.* **321**, 421–441.

Mei, R. & Klausner, J. F. 1992 Unsteady force on a spherical bubble at finite Reynolds number with small fluctuations in the free-stream velocity. *Phys. Fluids* **4**, 63–70.

Moore, W. D. 1965 The velocity of rise of distorted gas bubbles in a liquid of small viscosity. *J. Fluid Mech.* **23**, 749–766.

Philippi, P. C., Hegele, L. A. Jr., dos Santos, L. O. E. & Surmas, R. 2006 From the continuous to the lattice Boltzmann equation: The discretization problem and thermal models. *Phys. Rev.* E **73**, 056702.

Riboux, G., Risso, F. & Legendre, D. 2010 Experimental characterization of the agitation generated by bubbles rising at high Reynolds number. *J. Fluid Mech.* **643**, 509–539.

Roma, A. M., Peskin, C. S. & Berger, M. J. 1999 An adaptive version of the immersed boundary method. *J. Comput Phys.* **153**, 509–534.

Sangani, A. S. & Acrivos, A. 1983 Creeping flow through cubic arrays of spherical bubbles. *Intl J. Multiphase Flow* **9**, 181–185.

Sangani, A. S. & Didwania, A. K. 1993 Dynamic simulations of flows of bubbly liquids at large Reynolds numbers. *J. Fluid Mech.* **250**, 307–337.

Shan, X., Yuan, X.-F. & Chen, H. 2006 Kinetic theory representation of hydrodynamics: a way beyond the Navier–Stokes equation. *J. Fluid Mech.* **550**, 413–441.

Somers, J. A. 1993 Direct simulation of fluid flow with cellular automata and the lattice-Boltzmann equation. *Appl. Sci. Res.* **51** (1/2), 127.

Ten Cate, A., Deksen, J. J., Portela, L. M. & Van Den Akker, H. E. A. 2004 Fully resolved simulations of colliding monodisperse spheres in forced isotropic turbulence. *J. Fluid Mech.* **519**, 233.

Uhlmann, M. 2005 An immersed boundary method with direct forcing for the simulation of particulate flows. *J. Comput. Phys.* **209**, 448–476.

Uhlmann, M. 2008 Interface-resolved direct numerical simulation of vertical particulate channel flow in the turbulent regime. *Phys. Fluids* **20**, 053305.

Van Sint Annaland, M., Dijkhuizen, W., Deen, N. G. & Kuipers, J. A. M. 2006 Numerical simulation of behavior of gas bubbles using a 3-D front-tracking method. *AIChE J.* **52**, 99–110.

Yin, X. & Koch, D. L. 2008 Lattice-Boltzmann simulation of finite Reynolds number buoyancy-driven bubbly flows in periodic and wall-bounded domains. *Phys. Fluids* **20**, 103304.

Zenit, R., Koch, D. L. & Sangani, A. S. 2001 Measurements of the average properties of a suspension of bubbles rising in a vertical channel. *J. Fluid Mech.* **429**, 307–342.